PAPER

Check for updates

Synchrotron macro ATR-FTIR micro-spectroscopy to unlock silver ion-induced biochemical alterations in bacteria†

Tien Thanh Nguyen, [iD] ‡[ab] Ngoc Huu Nguyen, [iD] ‡[bc] Giang Tuyet Pham,[b] Jitraporn Vongsvivut, [iD] [d] Melissa H. Brown, [iD] [e] Vi Khanh Truong [iD] *[b] and Krasimir Vasilev [iD] *[b]

Bacterial infections are recognized as the leading cause of death for millions of individuals worldwide. There has been a growing research focused on antimicrobial materials that can provide alternatives to antibiotics. Among these, silver has emerged as a promising antibacterial agent, owing to its remarkable antimicrobial properties. However, the antimicrobial mechanisms of silver ions are still being debated. This study aimed to investigate biochemical and morphological changes that occur in two prevalent pathogenic bacterial cell types following treatment with silver ions. Using synchrotron macro-attenuated total reflection-Fourier transform infrared (ATR-FTIR) micro-spectroscopy and high-resolution micro-scopy, significant alterations in the protein (amide I and amide II) and phospholipid structural components of both bacterial species after silver treatment could be observed. More subtle modifications of *Staphylococcus aureus* were observed in the polysaccharide and nucleic acid regions than *Pseudomonas aeruginosa*. These structural variations can be attributed to the potent chemical interactions between silver ions and the thick cell wall of *S. aureus*. The findings of this research shed light on the antibacterial mechanisms induced by silver ions, offering a fresh perspective through the utilization of synchrotron ATR-FTIR for the identification of these mechanisms. This study contributes to our understanding of the applications of silver ions in combating infections and provides a foundation for further investigations towards developing more effective antibacterial agents and treatments.

Introduction

In 2019, a staggering 7.7 million deaths worldwide were recorded as a result of infections caused by 33 distinct types of pathogenic bacteria.[1] Among these, antibiotic-resistant strains significantly contributed to the severity of the situation, with approximately 4.95 million fatalities linked to antimicrobial resistance.[2] This constitutes a pressing global challenge that demands immediate attention. Currently, antibiotic treatment remains the most efficient, safe, and widely practiced approach for combating infections. Nevertheless, the excessive use of antibiotics has engendered the emergence and proliferation of antibiotic-resistant bacteria, while the development of novel antibiotics has struggled to keep up with the rate of development of resistant variants.[1,3] Consequently, there is a heightened focus among the scientific and medical communities on researching novel antimicrobial agents.[4–7]

Silver ions are a promising candidate which have garnered increasing attention as a potential antimicrobial agent.[8–10] These ions possess the ability to effectively combat various types of microorganisms, even at low concentrations.[8,11,12] Previous studies utilizing diverse analytical techniques have revealed that silver ions exert their antimicrobial effects through multiple mechanisms, including disruption of cell membranes, damage to genetic material, generation of intra-cellular reactive oxygen species, and more.[13–15] Despite con-siderable research, the intricate biochemical interactions between silver ions and microbial cell membranes have not been comprehensively elucidated.[13,16] This indicates a signifi-cant knowledge gap that warrants thorough investigation,

[a] College of Medicine and Pharmacy, Tra Vinh University, Tra Vinh 87000, Vietnam

[b] Biomedical Nanoengineering Laboratory, College of Medicine and Public Health, Flinders University, Bedford Park, SA 5042, Australia.
E-mail: Krasimir.vasilev@flinders.edu.au, vikhanh.truong@flinders.edu.au

[c] School of Biomedical Engineering, University of Sydney, Darlington, NSW 2006, Australia

[d] Infrared Microspectroscopy Beamline, ANSTO Australian Synchrotron, Clayton, VIC 3168, Australia

[e] College of Science and Engineering, Flinders University, Bedford Park, SA 5042, Australia

† Electronic supplementary information (ESI) available. See DOI: https://doi.org/10.1039/d3ma00598d

‡ Equal contribution.

especially with respect to the interaction of Ag^+ at the bio-interface.

Quantifying chemical interactions occurring at the biological interface between bacterial cells and silver ions is challenging, especially in the context of living organisms. The Fourier transform infrared spectroscopy (FTIR) technique is a powerful spectroscopic method employed to identify variations in the complete composition of microorganisms. It enables the detection and analysis of molecular signatures present in bacterial composition through the absorption of infrared energy. By revealing changes in the functional groups of biomolecules, FTIR enables precise analysis of microorganisms and their constituents[17–19] through identifying the rotational degree and characteristic movement of biochemical bonds, including those in proteins, phospholipids, polysaccharides, and nucleic acids.[18–20] Nonetheless, traditional FTIR instruments have inherent limitations in terms of their resolution, preventing them from effectively investigating subcellular events within smaller biological systems like bacteria.

In this pioneering research, we employed the cutting-edge synchrotron macro-attenuated total reflection (ATR)-FTIR micro-spectroscopy to probe the intricate biochemical alterations instigated by silver ions within two pathogenic bacteria, Gram-positive *Staphylococcus aureus* and Gram-negative *Pseudomonas aeruginosa*. We chose silver ions for this study due to their renowned efficacy and broad-spectrum antimicrobial activity, even at low concentrations, which is a significant advantage over other antimicrobial agents. Their unique ability to target multiple cellular components simultaneously minimizes the potential for the development of bacterial resistance, distinguishing them as a superior choice in antimicrobial research. The advanced synchrotron macro ATR-FTIR micro-spectroscopy enables a more comprehensive and detailed understanding of these changes at the sub-cellular level, which

is impossible with conventional FTIR instruments. Furthermore, it offers unparalleled insights into the multifaceted interactions between silver ions and microbial cell membranes and detailed mappings of biochemical interfaces within cell substructures. This method stands out concerning traditional techniques by enabling us to investigate multiple mechanisms of action concurrently rather than exploring each one sequentially.[21]

Our innovative approach provided us with an unprecedented view of cellular deformations, protein denaturation, and modifications to the structures of polysaccharides and nucleic acids, all triggered by the interaction with silver ions (Fig. 1). To achieve this, we employed a combination of optical techniques and macro ATR-FTIR micro-spectroscopy. The visualization of bacterial structures post-treatment with silver ions was carried out using scanning electron microscopy (SEM) and confocal laser scanning microscopy (CLSM). By employing high-resolution ATR-FTIR spatial hyperspectral imaging, we successfully mapped the biochemical interfaces within the cell substructures of both control and treated bacterial cell samples. This highlighted discernible variations when comparing the two systems.[21,22] To analyze the changes in cellular components, we focused on specific spectral regions. These regions involved the analysis of methylene groups (3000–2800 cm^{-1}), amide I and II (1705–1500 cm^{-1}), as well as regions associated with nucleic acids and polysaccharides (1200–950 cm^{-1}).[22–24] Vibrational peaks observed in the methylene regions are frequently linked to the phospholipid membrane of cellular structures. The amide I and II bands are utilized for the identification of microbial cells, as these vibration patterns correspond to proteins.[20,21,23] In the specific region, there are two specific ranges of significant importance. The nucleic acid region (1200–1075 cm^{-1}) is closely associated with the DNA and RNA of cells, whereas the polysaccharide bands (1150–900 cm^{-1}) can be attributed to structural polysaccharides, such as
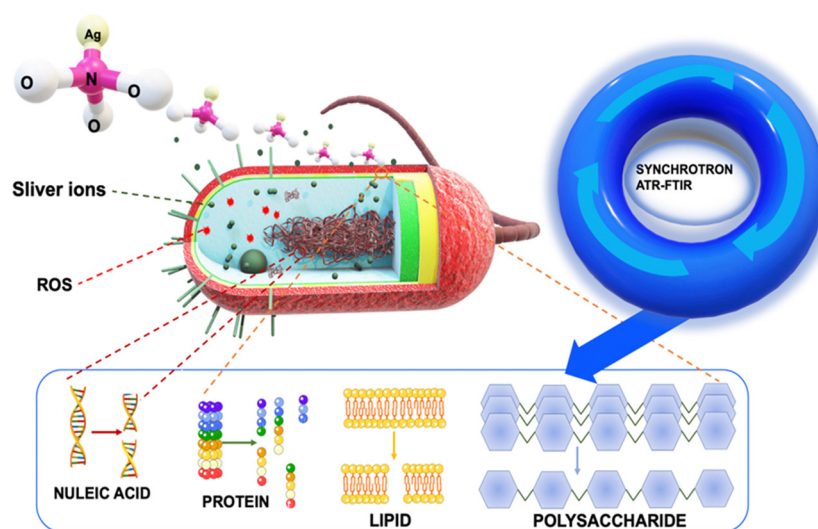

Fig. 1 Schematic illustrating the use of synchrotron macro ATR–FTIR micro-spectroscopy to reveal the antibacterial mechanism of silver ions against *S. aureus* and *P. aeruginosa*. The diagram demonstrates how silver ions generate reactive oxygen species (ROS), which subsequently alter the lipid, protein, nucleic acids, and polysaccharide compositions, ultimately leading to bacterial cell death.

peptidoglycan, found throughout the cell and its wall.[22–25] Then, principal component analysis (PCA) was used to determine the resemblances and fluctuations in the comparing process between treated and untreated samples related to cell spectral maps. We employed the extended multiplicative scatter correction (EMSC) method to analyze the chemical composition changes in cells when exposed to silver ions, thereby highlighting the important alterations that occur during sample processing with silver ions. The obtained results offer valuable insights into the impact of silver ions on the modification and disruption of bacterial structures, including the cell membrane, phospholipids, proteins, and nucleic acids. The novel insights garnered from the unique application of synchrotron macro ATR-FTIR micro-spectroscopy not only illuminate the multifaceted antimicrobial activity of silver ions but also set the stage for crafting more sophisticated and effective antibacterial strategies in the future.

Methods

Bacterial preparation

The bacterial strains *S. aureus* ATCC 25923 and *P. aeruginosa* ATCC 15692 were chosen to represent pathogenic Gram-positive and Gram-negative bacteria, respectively. Prior to each experiment, the bacterial cultures were cultivated on tryptone soy agar (TSA) (Sigma-Aldrich, Australia). Cultures were allowed to grow overnight at a temperature of 37 °C. Subsequently, a single bacterial colony was carefully selected from each culture and cultured in TSB under static conditions overnight at 37 °C. The density of the cultures was collected during the logarithmic growth phase.

Minimum inhibitory concentration and minimum bactericidal concentration determination

The MIC of AgNO$_3$ against the test bacteria was determined using a 96-well microplate. A dilution series was created, starting at 1 mg, of AgNO$_3$ in a sterile medium, and going all the way down to 0.015 mg. The wells were then seeded with 20 microliters of a bacterial culture of *P. aeruginosa* and *S. aureus* at a density of 10^6 CFU mL^{-1}. A control group was maintained without AgNO$_3$. Inoculated cultures were incubated at 37 °C in 24 hours before being measured by using plate reading.

Following identifying the minimum inhibitory concentration (MIC) of the silver ions, we extracted 50 μL portions from all tubes that showed no signs of bacterial development. These aliquots were then cultured on TSA plates and left to incubate at 37 °C for a 24 hour period. Bactericidal activity of samples is represented by the minimum effective concentration (MBC), which is the concentration at which all bacterial cells are killed.

Live/dead staining

SYTO® 9 and propidium iodide (PI) (Live/dead™ BacLight™, L7007 USA) were mixed at a 1:1 ratio, and used to stain the 10^6 CFU mL^{-1} bacterial solutions (treated and untreated with silver ions) for 10 minutes. Confocal laser scanning microscopy (Zeiss LSM880, Oberkochen, Germany) was used to determine the percentage of dead bacteria. Zen Blue and Fiji were used for the quantification of the data. All experiment was triplicated.

Antibacterial percentage was calculated as: (number of dead bacteria)/(total number of bacteria) × 100%.

Scanning electron microscopy characterisation

After incubation with the silver ions, the bacteria cells were preserved in 4% glutaraldehyde for 1 hour at room temperature. Subsequent dehydration was accomplished by immersing the samples in ethanol solutions ranging in concentration from 30% to 100%. The samples were then coated with 2 nm of platinum. The FEI Inspect F50 (FEI Company, Oregon, USA) was used to make the observations at 5 kV and a working distance of 5 mm.

Reactive oxygen species determination

To conduct the assay, 100 mL of a diluted solution of 2′,7′-dichlorofluorescin diacetate (DCF-DA) (Abcam, Australia), was added to each well (containing untreated and treated bacterial solutions) and incubated at 37 °C in the dark for 45 minutes. As a positive control, untreated samples of bacteria were exposed to *tert*-butyl hydroperoxide (TBHP). By monitoring the fluorescence intensity (FI) at 485/535 nm using a confocal laser scanning microscope (CLSM), the relative ROS quantity was determined.

Synchrotron ATR-FTIR operation and data analysis

ATR-FTIR mapping was used to examine the spatial distribution of chemical functional groups in untreated samples and those treated with AgNO$_3$. This investigation was performed at the Infrared Micro-spectroscopy (IRM) beamline at the Australian Synchrotron, using a Bruker Hyperion 3000 FTIR microscope connected to a VERTEX V80v FTIR spectrometer (Bruker Optik GmbH, Ettlingen, Germany).[26] We incorporated a specialized macro ATR-FTIR device that featured a germanium (Ge) ATR crystal with a 250 μm diameter (n_{Ge} = 4.0) and a 20× IR objective (NA = 0.60). The bacterial samples were meticulously mounted on CaF$_2$ surface and subsequently air-dried to ensure the absence of water, which could interfere with the analysis. Following this, the CaF$_2$ surface bearing the samples was positioned on aluminum discs to perform the ATR-FTIR analysis. We managed spectral parameters, such as a spectral range of 3900–950 cm^{-1} and a spectral resolution of 4 cm^{-1}, using Bruker's OPUS 8.0 software suite. The spectrum of water vapor was subtracted from the sample spectra to minimize the influence of residual water. A background spectrum was collected under the same conditions to ensure the accuracy of the subtraction. The software also facilitated the generation of chemical maps by integrating the area beneath the appropriate peaks in the spectra. We used CytoSpec v. 1.4.02 (Cytospec Inc., Boston, MA, USA) and the UnscramblerX 11.1 software package (CAMO Software AS, Oslo, Norway) to conduct advanced multivariate data analysis.

Results and discussion

Antibacterial properties of silver ions against Gram-positive and Gram-negative pathogenic bacteria

The antimicrobial efficacy of the suspension of silver nitrate against two model microbial species was conducted using *S. aureus* (ATCC 25923) and *P. aeruginosa* (ATCC 15692). The bactericidal and bacteriostatic activity of silver ion against pathogenic bacteria was determined using minimum inhibitory concentration (MIC) and minimum bactericidal concentration (MBC) assay. As shown in Table 1, silver ion was effective against both *S. aureus* and *P. aeruginosa*, with MIC values of 1.5 mM and 0.09 mM, respectively, and MBC values of 3 mM and 0.18 mM, respectively. This result is consistent with previous studies.[27–30]

By utilizing live and dead fluorescent staining and employing the determined MIC concentrations, we could effectively evaluate the antibacterial resistance capacity of two specific disease-causing bacterial strains against silver ions. The differentiation between living and deceased cells was established through the application of a staining method alongside confocal laser scanning microscopy (CLSM). The staining process involved using SYTO® 9, which imparted a green hue to the bacterial cells, and propidium iodide (PI), which caused the cells to appear red. The SYTO® 9 stain is typically used to label living bacteria and can passively diffuse into bacterial cells, whereas PI is only able to enter bacteria with permeabilized membranes and is commonly associated with dead or dying cells.[31,32]

The percentage of bacterial cells that died in untreated bacterial samples was 1.6% and 1.3% for *S. aureus* and *P. aeruginosa*, respectively. In contrast, bacterial samples treated with silver nitrate at their MIC had a mortality rate of approximately 99.9% for both types of bacteria (Fig. 2). These findings are consistent with previous research reports.[13]

Silver ions promoting intracellular reactive oxygen species (ROS) production and inducing morphological alterations in bacterial cells

To enhance our comprehension of the antibacterial properties of silver ions, we undertook further studies by examining the presence of reactive oxygen species (ROS) and bacterial morphologies with scanning electron microscopy. ROS generation in bacteria indicates the antimicrobial activity of silver ions.[33,34] ROS were detected by using a fluorescent dye (DCFDA/H2DCFDA-Cellular ROS Assay Kit). As shown in Fig. 3a, green fluorescence signals were observed in both bacterial species cultured in solution containing silver ion, with higher fluorescence intensity indicating higher concentrations of intracellular ROS.
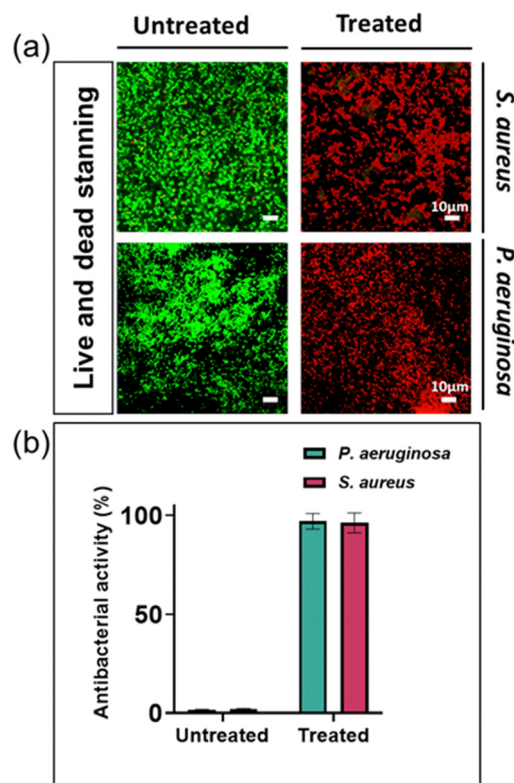

Fig. 2 Evaluation of silver ions' antibacterial efficacy against *S. aureus* and *P. aeruginosa*. (a) Confocal laser scanning microscopy images displaying bacterial interaction with 0.74 mM silver ions for *S. aureus* and *P. aeruginosa* respectively. (b) Quantitative assessment of antibacterial activity illustrated through graphical data representation. Scale bar = 10 μm. Data are presented as mean ± standard deviation. *n* = 3.

Based on Fig. 3b, the fluorescence signal intensity detected in *S. aureus* treated with Ag$^+$ is significantly higher than in *P. aeruginosa*. These findings demonstrate that silver ions have triggered the generation of intracellular ROS in the bacterial cells.

We used SEM to study morphology of these two bacterial species after being exposed for 24 hours to AgNO$_3$ at the MIC concentration. The results indicated significant alterations in the bacterial structure and shape compared to healthy (control) cells, as both the cell membrane structure and the overall bacterial architecture appeared almost entirely disrupted (Fig. 3c). Observations of the bacterial cell membrane integrity indicated that it was completely compromised, leading to the extrusion of the bacterial cytoplasm. This suggests that silver ions trigger the formation of ROS, resulting in disrupting the cell membrane, leading to bacterial cell death through several pathways, including damage to the cell membrane, interaction with nucleic acids, and disruption of bacterial proteins, consistent with findings in multiple published studies.[13,35,36]

Analysis of the interaction between silver ions and bacteria using macro ATR-FTIR micro-spectroscopy

To elucidate the antibacterial mechanisms of silver ions, we employed an advanced analytical technique known as ATR-FTIR micro-spectroscopy. This technique allowed us to capture
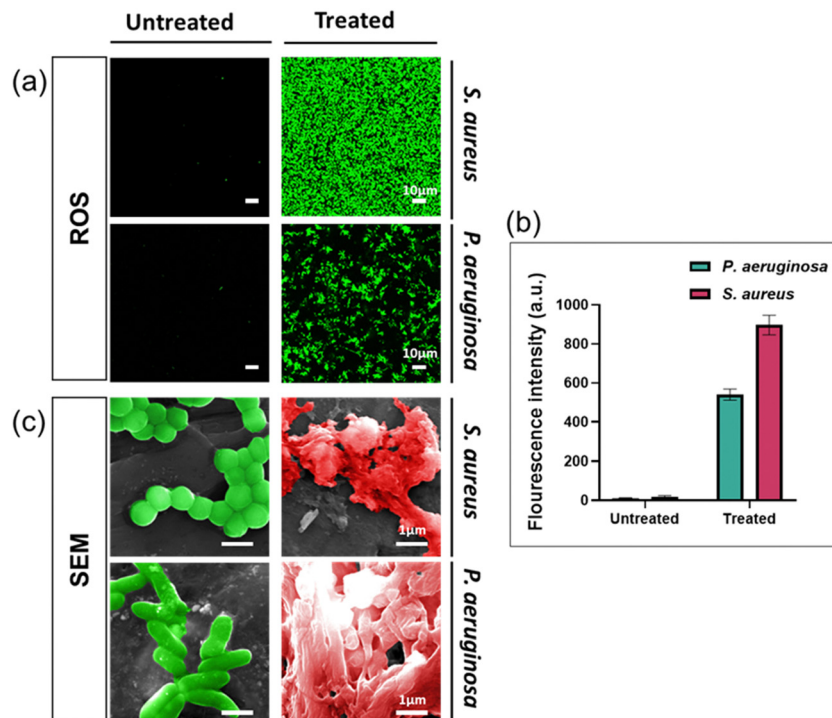
Table 1 Minimum inhibitory concentration (MIC) and minimum bactericidal concentration (MBC) of silver ions against Gram-positive and Gram-negative bacteria

Bacterial strains	MIC (mM)	MBC (mM)
Pseudomonas aeruginosa ATCC 15692	0.09	0.18
Staphylococcus aureus ATCC 25923	0.74	1.5

Fig. 3 Determination of silver ions' antibacterial mechanism against *S. aureus* and *P. aeruginosa*. (a) Confocal laser scanning microscopy (CLSM) images demonstrating bacterial ROS interacting with silver ions. Scale bar = 10 μm, magnification = 63×. (b) Quantitative assessment of ROS intensity illustrated through graphical data representation. Data are presented as mean ± standard deviation. (c) SEM images showing the morphological changes of bacteria after exposure to silver ions. Scale bar = 1 μm. *n* = 3.

changes in bacterial structural molecules, as reflected in the spectra obtained from the synchrotron macro ATR-FTIR micro-spectroscopy system, thus providing comparative analyses of their alterations.

High-resolution ATR-FTIR micro-spectroscopy synchrotron maps were collected to investigate the biochemical interactions of silver ions with both Gram-negative and Gram-positive bacterial cells. Specifically, to delve into the structural changes of the molecules within the cell membrane and bacterial nucleus, we selected key spectral regions, including the methylene region (3000–2800 cm^{-1}) for lipids, the amide region (1705–1600 cm^{-1}) for proteins, and a specific area (1200–950 cm^{-1}) for polysaccharides and nucleic acids changes.

From the obtained spectral data, we constructed tables representing these spectral regions. In Fig. 4, they are represented as a function of the FTIR absorption intensity, estimated by integrating data across the designated spectral region.[25,37,38] These provide a direct and accurate visualization of spectral data in actual space.

In Fig. 4, the overlapping regions with high intensity identified in the spectral ranges of 3000–2800 cm^{-1} and 1705–1600 cm^{-1}, respectively, represent points indicating the presence of abundant lipid and protein content.[20,39] In the lower wavenumber range of 1200–1000 cm^{-1}, polysaccharides, which constitute the structural components of bacterial cells, are indicated. In the FTIR maps, the intense mixed signals of lipids and proteins are considered as the accumulation sites in

bacterial cells. This holds significance as it underscores the impressive resolution of the technique while firmly establishing the feasibility of attaining subcellular spectral analysis.

The images of spectral maps provide crucial information about the spectral distribution of functional groups belonging to bacteria of interest. Identifying the differences in the spectra representing these groups can help determine the structural changes in bacteria after they have been exposed to silver ions.

For the untreated sample, the spectral overlap of the –CH and amide functional groups is relatively similar. The spectra of polysaccharides are more broadly distributed, but overlapping locations still reside at points of high-intensity amides and lipids. These spectra are concentrated in the same areas that can be identified on the spectral maps. Conversely, the spectral maps present a different distribution of the functional groups for samples treated with silver ions when compared with untreated samples. The treated samples exhibit a reduction in overlapping points and an increase in more distinct signals in the –CH and amide spectral regions. This supports the idea that exposure to silver ions results in bacterial cell degradation, exposing intracellular components in bacteria such as lipids and proteins. This is supported by the changes in bacterial structure observed in the SEM images (Fig. 3c).

To gain a statistical perspective on the differences in spectral maps, we conducted hierarchical cluster analysis (HCA) to group regions with similar spectra. The selected spectral ranges for analysis included protein–polysaccharide-nucleic
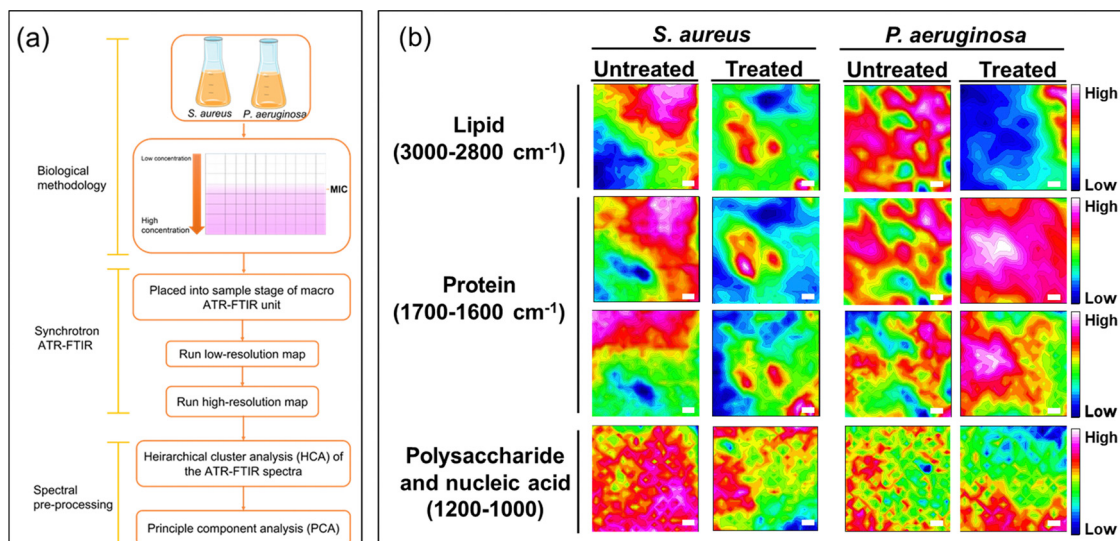
Fig. 4 Illustration of biochemical changes in *S. aureus* and *P. aeruginosa* cells as detected by synchrotron macro-ATR-FTIR. (a) Schematic representation of the synchrotron macro ATR-FTIR operation. (b) The heat maps depict the variation of lipids, proteins, nucleic acid and polysaccharides within the cells. The white scale bars correspond to a length of 5 μm.

acid (1810–1000 cm^{-1}) and lipid (3004–2810 cm^{-1}) spectra. The second derivative was utilized to highlight the prominent spectral regions as it represents the overall rate of spectral change.[40,41]

Subsequently, five spectral plots were generated based on the average spectral values of clusters exhibiting similar spectral patterns. To determine the dominant average spectra for use in PCA, we compared and selected the cluster(s) with the largest area coverage in the spectral map. Additionally, the selected cluster's average spectrum should exhibit the highest peak intensities and lowest noise levels among functional groups, including amide I and –CH stretching. They were chosen because they have the highest distinct peaks for determining the presence of cells. These standards were employed to choose a cluster that comprised cells, enabling comparisons between the untreated and treated samples.[20,21,37]

To analyze and identify significant changes in the recorded spectral system observed by the synchrotron macro ATR-FTIR system between untreated and treated samples, we performed HCA as mentioned earlier. Before processing the spectra by EMSC, all spectra belonging to the spectral cluster were first subjected to a second-derivative transformation. Subsequently, the combined set of spectra underwent PCA to explore the similarities and distinctions among the cell groups.[20,21] The PCA scores for the principal components, namely PC-1, PC-2, and PC-3, were calculated and displayed in Fig. 5a and 6a. These scores were utilized to elucidate the differences between the untreated and silver ion-treated cell samples.

Fig. 5a demonstrates a notable dissimilarity between the two samples, with PC-1 and PC-2 accounting for 95% and 4% of the observed variation, respectively. This indicates a significant change when the Gram-positive bacterium *S. aureus* was subjected to silver ion treatment. The PCA score plot reveals a clustered distribution of scores for the untreated samples along
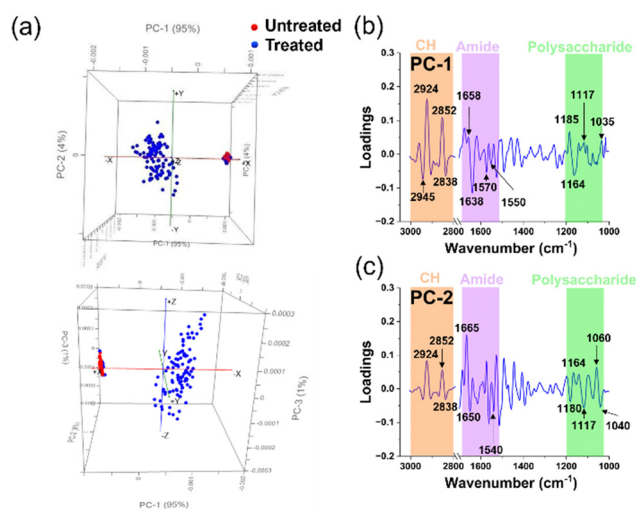

Fig. 5 Principal component analysis (PCA) of untreated and treated *S. aureus* cells. (a) Comparative PCA score plots for untreated and treated *S. aureus* cells. (b) and (c) PCA loading spectra correlations between PC-1 and PC-2 scores for untreated and treated groups in each microbial cell population. The peaks of interest and their corresponding assignments are summarised in Table 2.

PC-1 and PC-2, while the scores representing the treated samples appear more scattered. Based on the PCA characteristics, it can be inferred that the tight clustering of PCA scores in the untreated samples results from the similarity in the biochemical structural composition of the cellular constituents. In contrast, the scattered distribution suggests a lack of similarity in the biochemical structures among the cells, indicating that the cells have undergone transformation or degradation.[20,21] Additionally, we observed minimal overlap between the treated and untreated samples. However, these few instances do not diminish the noteworthy changes in the
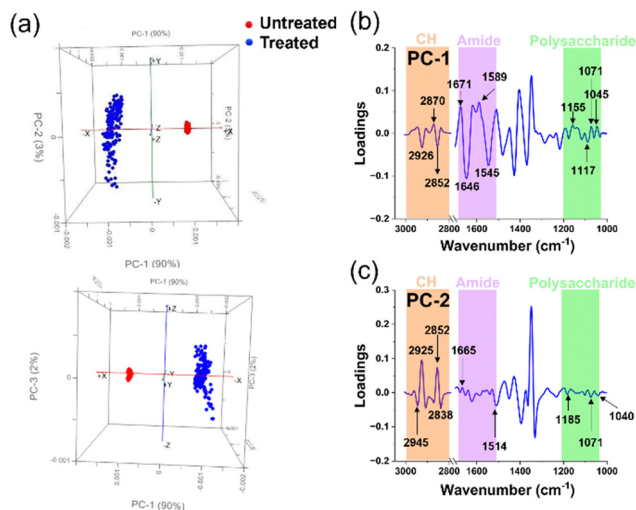
Fig. 6 Principal Component Analysis of untreated and treated *P. aeruginosa* cells. (a) Comparative PCA score plots for untreated and treated *P. aeruginosa* cells. (b) and (c) PCA loading spectra correlations between PC-1 and PC-2 scores for untreated and treated groups in each microbial cell population. The peaks of interest and their corresponding assignments are summarised in Table 2.

chemical components of bacterial cell functional groups caused by silver ions. To further explore the changes in the chemical structure of functional groups between the untreated and treated samples, we further utilized the PCA loadings, particularly PC-1 and PC-2. The magnitude of the load peaks can signal the extent of disparity, where greater magnitudes indicate apparent variations. The significant peaks are emphasized in Fig. 5b, c, and the related biochemical substances have been identified in the ESI† tables. A summary of these findings can be found in Table 2.

The interaction between *S. aureus* cells and silver ions is elucidated through the PCA loadings in PC-1. The loading plot highlights that most of the peaks with significant intensity are concentrated within the lipid region. Specifically, two peaks of high intensity are observed in the lipid region, suggesting possible alterations in the methylene groups within the phospholipid structure that constitutes the cell membrane.[22,25] Subsequently, peaks with elevated intensity are predominantly located in the amide I and amide II regions, indicating structural modifications in proteins within the treated samples.[24,25,38] Noteworthy, changes in the cell membrane can also be discerned by peaks within the polysaccharide and nucleic acid region.[25]

In contrast to the high intensity of peaks in the lipid region of the PC-1 loading, the PC-2 loading spectra of *S. aureus* showed greater intensity peaks located at amide I and amid II regions.[20,22,24] The latter suggests that changes of protein in bacterial cells occurred.

The alterations in the lipid functional groups within the cellular membrane continue to be loaded in the PC-2 spectra through discernible peaks in the lipid region (Fig. 5c). The prominent escalation of peaks within the amide I, amide II, and lipid regions, observed in both PC-1 and PC-2 spectra, signifies

the influence of silver ions on the protein and lipid structures within the bacterial cell membrane. Furthermore, the emergence of bends is also evident through peaks in the polysaccharide and nucleic acid region.[23,25] The polysaccharides are known to be allocated to the capsule layer and thick cell wall (peptidoglycan layer) of Gram-positive *S. aureus*.[44] Therefore, the variations in the spectral properties within this polysaccharide range provide compelling evidence of significant changes occurring in the bacterial cell membrane following silver ion treatment. These changes suggest a potential loss of structural integrity in the cell membrane, as clearly observed through the utilization of SEM images in Fig. 3c. Additionally, we observed prominent peaks in the PC-2 loading, indicating alterations in the nucleic acid structure of the cells.[23,25] These changes could potentially arise from the integration process involving Ag^+ (and $O_2^{\bullet-}$ radicals), leading to the generation of highly reactive hydroxyl radicals ($OH^\bullet$).[45,46] ROS possess the capability to selectively affect cellular biomolecules, thereby giving rise to oxidative stress. This consequential process can instigate detrimental consequences, such as DNA damage, inhibition of replication, and disruption of RNA functionality.[15,45] Indeed, ROS were detected in the *S. aureus* cells using fluorescence staining and quantified through CLMS imaging (Fig. 3a). The intensity of ROS was found to be significantly higher than the control, registering at levels above 850 a.u.

The PCA score plots of the untreated and treated groups for *P. aeruginosa* (Fig. 6a) unveiled distinct differences between the two groups, as evidenced by the respective 90% and 3% contributions of PC-1 and PC-2. These significant alterations within the cellular structure ensued following exposure to Ag^+ solution, an observation closely mirroring that made in the Gram-positive bacterium *S. aureus*. This similarity is likely due to the congruent cellular architecture of these two bacterial strains.[47,48]

In the PCA score distribution (Fig. 6a), untreated cell samples exhibited clustered PCA points. Conversely, PCA points of treated cell samples presented a broad scatter between PC-1 and PC-2. This disparity may be attributed to the structural disarray instigated by the silver ions' intervention, leading to cell destruction and diverse variation. Further, to elucidate the precise alterations in the cellular functional groups, we extended the use of PC-1 and PC-2 loadings (Fig. 6b and c) to investigate the characteristic disparities between the Ag^+ treated and untreated samples.

The interaction between *P. aeruginosa* cells and silver ions was elucidated *via* the PCA loads in PC-1. The load plot accentuated several prominent peaks within the amide I and II regions, alluding to modifications in cellular proteins.[22–25] Specifically, two pronounced peaks in the protein region signified alterations in the β-sheet bonds of amide I and δ_{N-H}, ν_{C-N} bonds of amide II, integral to the protein cellular structure. Lipids were the subsequent focus, with CH_2 stretching bonds apparent, suggesting lipid bond degradation in the cell membrane and protein alteration upon silver ion interaction.[22,25] The alterations indicate a possible compromise in the stability of the cellular membrane, which is clearly shown in Fig. 3c

Table 2 Summary of significant wavenumbers detected in the loading plots for *S. aureus* and *P. aeruginosa* subsequent to silver ion exposure

Bacterial species	PC	Wavenumber (cm^{-1})	Assignment	Ref.
S. aureus	1	2945–2836	C–H stretching from methylene (–CH$_2$) groups, acyl chains and aliphatic alkanes in the lipids	22, 24 and 25
		1673–1638	Amide I: anti-parallel β-sheet and α-helical structure of amide I ν(C=O) of carboxylate and ν(C=C) of aromatic compounds	22, 23 and 25
		1570–1550	Amide II: perpendicular modes of the α-helix and antiparallel β-sheet	22 and 25
		1185–1060	CH$_2$	24 and 25
			C–O propionates and higher esters, formats	
			ν(CO) stretching coupled with C–O mainly from the C–O stretching mode of C–OH groups	
		1035	Skeletal trans conformation (CC) of DNA	25
	2	2924–2852	C–H stretching from methylene (–CH$_2$) groups, acyl chains and aliphatic alkanes in the lipids	22, 24 and 25
		1666–1650	Amide I: disordered structure-solvated	23 and 25
		1571–1540	Protein amide II absorption-predominately β-sheet of amide II	23 and 25
		1180	Amide III band region	25
		1164	C–O stretching ribose	25
		1117–1040	C–O stretching vibration of C–OH group of ribose (RNA)	23 and 25
			Stretching C–O deoxyribose	
			Symmetric PO$_2^-$ stretching in RNA and DNA	
P. aeruginosa	1	2925–2852	ν_{as}(C–H) from methylene (–CH$_2$) groups of lipids	22, 24 and 25
			ν_sCH$_3$	
			Stretching C–H, N–H	
			Symmetric stretching vibration of CH$_3$ of acyl chains (lipids)	
		1671–1648	Amide I: anti-parallel β-sheet C=O, C–N and N–H bond	22, 23, 25 and 42
		1545–1509	Amide II protein structures: α-helix and β-sheet	23, 25 and 43
		1155	ν_{as}(CO–O–C) of glycogen and nucleic acids (DNA and RNA)	22 and 25
			C–O stretching vibration	
		1117–1045	C–O stretching vibration of C–OH group of ribose (RNA)	23 and 25
			νC–O of proteins and carbohydrates	
			Phosphate I band for two different C–O vibrations of deoxyribose in DNA in disordering structure	
	2	2945–2836	ν_{as}(C–H) stretching from methylene (–CH$_2$) groups of lipids	22, 24 and 25
			ν_s CH$_3$	
			Stretching C–H, N–H	
			Symmetric stretching vibration of CH$_3$ of acyl chains (lipids)	
		1665	Amide I: α-helix	22, 24 and 25
		1514	Amide II: parallel mode of the α-helix	22
		1184	CH$_2$	25
		1071–1040	Phosphate I band for two different C–O vibrations of deoxyribose in DNA in disordering structure.	25

through the application of SEM images. Interestingly, *P. aeruginosa* displayed a more vigorous transformation in the amide I and II regions compared to *S. aureus*, as shown by the spectral intensity of these functional groups in PC-1, which may be due to the structural differences between the Gram-positive and Gram-negative bacterial envelops.[48]

Another notable change was discerned from the spectral peaks in the polysaccharide region, derived from C–O bonds in the polysaccharide structures.[22,25] This peptidoglycan layer, part of the bacterial cell membrane, exhibited lower spectral peak intensities in *P. aeruginosa* compared to *S. aureus*, likely owing to the comparatively thinner peptidoglycan layer in Gram-negative bacteria.[48] Concurrently, we observed changes in the PO$_2$ stretching bonds in nucleic acids, possibly due to silver ion induced nucleic acid structure destruction *via* the formation of intracellular ROS groups in bacteria.[36] Indeed, fluorescence staining was employed to identify ROS within *P. aeruginosa*, and their quantity was determined using CLMS imaging (Fig. 3a). The analysis revealed that the ROS levels were notably elevated compared to the control group (untreated),

surpassing the threshold of around 500 a.u. Additionally, In PC-2 loading, we observed prominent peaks indicating alterations in the lipid structure of the cells.[23,25] The spectral intensities found within key regions of interest, specifically those related to proteins and polysaccharides, are discernible, albeit with notably low intensity. These findings, which highlight the structural modifications in cells upon treatment with silver ions, corroborate those of prior studies that employed various analytical methods.[13,33,49,50] This not only validates our results but also extends our collective understanding of the multi-faceted influence exerted by silver ions on bacterial cells, thereby adding to a growing body of research.[13,14,51]

To illuminate the considerable transformations in the chemical constituents of bacterial cells subsequent to the silver ion treatment, we conducted an analysis on individual spectra extrapolated from second derivatives for both types of bacteria (as illustrated in Fig. 7 and 8). Pertaining to Fig. 7, distinct variances at spectral peaks, representative of lipid groups in *S. aureus*, are most prominently exhibited. This is evidenced by the heightened peak intensity in the system subjected to
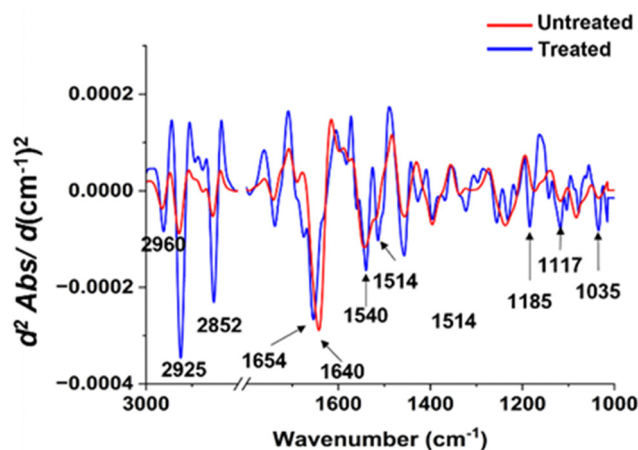
Fig. 7 Comparisons of the average EMSC-corrected second derivative spectra of the untreated and treated *S. aureus* with Ag ions.
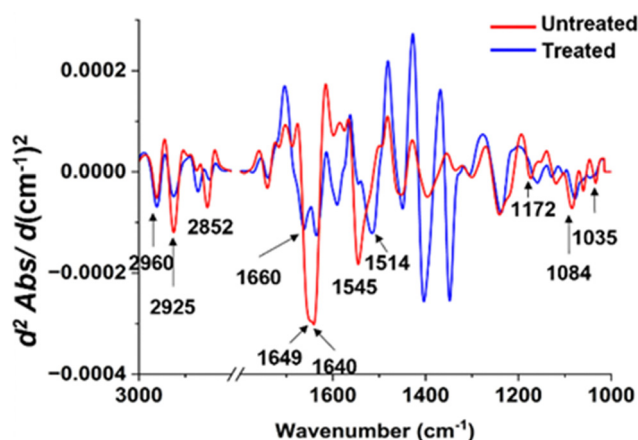

Fig. 8 Comparisons of the average EMSC-corrected 2nd derivative spectra of the untreated and treated *P. aeruginosa* with Ag ions.

treatment, as contrasted with the untreated system. In the realm of proteins, disparities were similarly observed. The spectral peaks of amide I demonstrated a subtle shift towards a larger numerical value, whereas the amide II band underwent morphological alteration and showed an increase in spectral intensity exceeding that of the untreated sample. Within the lipid domain, we observe a subtle transition towards an increased wavenumber, which may hint at intrinsic variations in the interactions occurring between silver ions and *S. aureus*. When considering the nucleic acid region, it is evident that there is a marked shift post-silver ion treatment. The spectral peak located at 1035 cm^{-1} presents an enhanced intensity, progressing towards a higher wavenumber subsequent to treatment.

In contrast to the distinct spectral variations observed in the lipid region of *S. aureus*, the protein region displayed the most noteworthy alterations in the *P. aeruginosa* sample exposed to silver ions (Fig. 7). The spectral peaks corresponding to the amide I region exhibited a significant reduction in intensity

following the treatment. Moreover, these peaks appeared more pronounced and demonstrated a slight shift towards higher wavenumbers. It is worth noting that the amide II region underwent substantial changes, characterized by a decrease in intensity and a spectral peak shift towards lower wavenumbers.

Regarding the lipid regions, a majority of the peaks experienced a decrease in intensity, with the exception of the peak at 2852 cm^{-1}, which shifted towards higher wavenumbers. The alterations were also evident in the polysaccharide regions, where the peaks exhibited a subtle increase in intensity and shifted towards lower wavenumbers compared to the untreated sample. Furthermore, the peaks within the nucleic acid region displayed a considerable decrease in intensity, notably the peak at 1084 cm^{-1}, which shifted towards lower wavenumbers. The combined findings from these spectra shed light on the specific cellular transformations that occur upon exposure to silver ions, offering valuable insights into the underlying antimicrobial mechanism of this chemical.

Silver ions have emerged as promising antibacterial agents in various medical material applications. Despite existing studies on the impact of silver ions on bacterial cells, many mechanisms are still under discussion. This study employed synchrotron macro ATR-FTIR and microscopy techniques to investigate the intricate biochemical interactions between silver ions and two prevalent pathogenic bacteria: *S. aureus* and *P. aeruginosa*.

Microscopic SEM and CLSM examinations revealed remarkable deformations in bacterial cells following exposure to silver ions. We generated ATR-FTIR spectral maps to elucidate the underlying biochemical transformations using the synchrotron as the primary light source. Comparing treated and untreated samples through principal component analysis targeting specific wavenumber regions associated with lipids, proteins, polysaccharides, and nucleic acids, our analysis unveiled the disruptive effect of silver ions on the cell membrane structure, corroborated by SEM and CLSM imaging. Furthermore, chemical changes in the amide I and amide II regions indicated protein denaturation in the treated bacterial samples. The impact of silver ions extended to polysaccharide and nucleic acid structures, manifested by subtle variations in spectral intensity and shifts in wavenumbers. Notably, the generation of intracellular ROS, resulting from the interaction with silver ions, was identified as one of the factors contributing to protein and nucleic acid degradation. These findings contribute to our understanding of the antimicrobial mechanism of silver ions and hold implications for the development of effective antibacterial treatments in the future.

Conclusions

In conclusion, the utilization of high-resolution ATR-FTIR with a synchrotron source has provided significant elucidation on the complex biochemical interaction between silver ions and bacterial cells. This valuable understanding has the potential to significantly impact the advancement of antimicrobial

treatments centered around silver ions, fostering the development of more effective and targeted therapeutic approaches.

Conflicts of interest

There are no conflicts to declare.

Acknowledgements

Notes and references

1 K. S. Ikuta, L. R. Swetschinski, G. Robles Aguilar, F. Sharara, T. Mestrovic, A. P. Gray, N. Davis Weaver, E. E. Wool, C. Han, A. Gershberg Hayoon, A. Aali and S. M. E. A. Abate, *Lancet*, 2022, **400**(10369), 2221–2248.

2 C. J. L. Murray, K. S. Ikuta, F. Sharara, L. Swetschinski, G. Robles Aguilar, A. Gray, C. Han, C. Bisignano, P. Rao, E. Wool, S. C. Johnson and A. J. E. A. Browne, *Lancet*, 2022, **399**(10325), 629–655.

3 M. S. Butler, V. Gigante, H. Sati, S. Paulin, L. Al-Sulaiman, J. H. Rex, P. Fernandes, C. A. Arias, M. Paul, G. E. Thwaites, L. Czaplewski, R. A. Alm, C. Lienhardt, M. Spigelman, L. L. Silver, N. Ohmagari, R. Kozlov, S. Harbarth and P. Beyer, *Antimicrob. Agents Chemother.*, 2022, **66**(3), e01991.

4 I. Banerjee, R. C. Pangule and R. S. Kane, *Adv. Mater.*, 2011, **23**(6), 690–718.

5 Z. Geng, R. Wang, X. Zhuo, Z. Li, Y. Huang, L. Ma, Z. Cui, S. Zhu, Y. Liang, Y. Liu, H. Bao, X. Li, Q. Huo, Z. Liu and X. Yang, *Mater. Sci. Eng., C*, 2017, **71**, 852–861.

6 A. Elbourne, S. Cheeseman, P. Atkin, N. P. Truong, N. Syed, A. Zavabeti, M. Mohiuddin, D. Esrafilzadeh, D. Cozzolino, C. F. McConville, M. D. Dickey, R. J. Crawford, K. Kalantar-Zadeh, J. Chapman, T. Daeneke and V. K. Truong, *ACS Nano*, 2020, **14**(1), 802–817.

7 K. Y. Kwon, S. Cheeseman, A. Frias-De-Diego, H. Hong, J. Yang, W. Jung, H. Yin, B. J. Murdoch, F. Scholle, N. Crook, E. Crisci, M. D. Dickey, V. K. Truong and T.-I. Kim, *Adv. Mater.*, 2021, **33**(45), 2104298.

8 A. Hamad, K. S. Khashan and A. Hadi, *J. Inorg. Organomet. Polym. Mater.*, 2020, **30**(12), 4811–4828.

9 S. Taheri, A. Cavallaro, S. N. Christo, L. E. Smith, P. Majewski, M. Barton, J. D. Hayball and K. Vasilev, *Biomaterials*, 2014, **35**(16), 4601–4609.

10 K. Prasad, G. S. Lekshmi, K. Ostrikov, V. Lussini, J. Blinco, M. Mohandas, K. Vasilev, S. Bottle, K. Bazaka and K. Ostrikov, *Sci. Rep.*, 2017, **7**(1), 1591.

11 A. Panáček, M. Kolář, R. Večeřová, R. Prucek, J. Soukupová, V. Kryštof, P. Hamal, R. Zbořil and L. Kvítek, *Biomaterials*, 2009, **30**(31), 6333–6340.

12 A. Panáček, L. Kvítek, R. Prucek, M. Kolář, R. Večeřová, N. Pizúrová, V. K. Sharma, T. J. Nevěčná and R. Zbořil, *J. Phys. Chem. B*, 2006, **110**(33), 16248–16253.

13 W. K. Jung, H. C. Koo, K. W. Kim, S. Shin, S. H. Kim and Y. H. Park, *Appl. Environ. Microbiol.*, 2008, **74**(7), 2171.

14 T. C. Dakal, A. Kumar, R. S. Majumdar and V. Yadav, *Front. Microbiol.*, 2016, 7.

15 A. Kędziora, M. Speruda, E. Krzyżewska, J. Rybka, A. Łukowiak and G. Bugla-Płoskońska, *Int. J. Mol. Sci.*, 2018, **19**, 444.

16 I. X. Yin, J. Zhang, I. S. Zhao, M. L. Mei, Q. Li and C. H. Chu, *Int. J. Nanomed.*, 2020, **15**, 2555–2562.

17 F. Faghihzadeh, N. M. Anaya, L. A. Schifman and V. Oyanedel-Craver, *Nanotechnol. Environ. Eng.*, 2016, **1**(1), 1.

18 I. Saraeva, E. Tolordava, S. Sheligyna, A. Nastulyavichus, R. Khmelnitskii, N. Pokryshkin, D. Khmelenin, S. Kudryashov, A. Ionin and A. Akhmatkhanov, *Int. J. Mol. Sci.*, 2023, **24**, 5119.

19 D. Bajrami, S. Fischer, H. Barth, M. A. Sarquis, V. M. Ladero, M. Fernández, M. C. Sportelli, N. Cioffi, C. Kranz and B. Mizaikoff, *npj Biofilms Microbiomes*, 2022, **8**(1), 92.

20 S. Cheeseman, Z. L. Shaw, J. Vongsvivut, R. J. Crawford, M. F. Dupont, K. J. Boyce, S. Gangadoo, S. J. Bryant, G. Bryant, D. Cozzolino, J. Chapman, A. Elbourne and V. K. Truong, *Molecules*, 2021, **26**, 3890.

21 J. Vongsvivut, D. Pérez-Guaita, B. R. Wood, P. Heraud, K. Khambatta, D. Hartnell, M. J. Hackett and M. J. Tobin, *Analyst*, 2019, **144**(10), 3226–3238.

22 J. Vongsvivut, P. Heraud, A. Gupta, M. Puri, D. McNaughton and C. J. Barrow, *Analyst*, 2013, **138**(20), 6016–6031.

23 S. J. Parikh and J. Chorover, *Langmuir*, 2006, **22**(20), 8492–8500.

24 J. Oberle, J. Dighton and G. Arbuckle-Keil, *Fungal Biol.*, 2015, **119**(11), 1100–1114.

25 Z. Movasaghi, S. Rehman and D. I. ur Rehman, *Appl. Spectrosc. Rev.*, 2008, **43**(2), 134–179.

26 J. Vongsvivut, D. Pérez-Guaita, B. R. Wood, P. Heraud, K. Khambatta, D. Hartnell, M. J. Hackett and M. J. Tobin, *Analyst*, 2019, **144**(10), 3226–3238.

27 P. Singh, S. Pandit, V. Mokkapati, J. Garnæs and I. Mijakovic, *Molecules*, 2020, **25**, 2783.

28 A. Pormohammad and R. J. Turner, *Antibiotics*, 2020, **9**, 853.

29 A. Pormohammad, A. Firrincieli, A. Salazar-Alemán Daniel, M. Mohammadi, D. Hansen, M. Cappelletti, D. Zannoni, M. Zarei and J. Turner Raymond, *Microbiol. Spectrum*, 2023, e00628.

30 H. D. Salman, *J. Global Pharma Technol.*, 2017, **9**, 238–248.

31 L. Boulos, M. Prévost, B. Barbeau, J. Coallier and R. Desjardins, *J. Microbiol. Methods*, 1999, **37**(1), 77–86.

32 S. M. Stocks, *Cytometry, Part A*, 2004, **61A**(2), 189–195.

33 A. Kędziora, R. Wieczorek, M. Speruda, I. Matolínová, T. M. Goszczyński, I. Litwin, V. Matolín and G. Bugla-Płoskońska, *Front. Microbiol.*, 2021, 12.

34 H.-J. Park, J. Y. Kim, J. Kim, J.-H. Lee, J.-S. Hahn, M. B. Gu and J. Yoon, *Water Res.*, 2009, **43**(4), 1027–1032.

35 Y. Yakabe, T. Sano, H. Ushio and T. Yasunaga, *Chem. Lett.*, 1980, (4), 373–376.

36 O. McNeilly, R. Mann, M. Hamidian and C. Gunawan, *Front. Microbiol.*, 2021, **12**.

37 D. Q. Pham, S. J. Bryant, S. Cheeseman, L. Z. Y. Huang, G. Bryant, M. F. Dupont, J. Chapman, C. C. Berndt, J. Vongsvivut, R. J. Crawford, V. K. Truong, A. S. M. Ang and A. Elbourne, *Nanoscale*, 2020, **12**(38), 19888–19904.

38 W. Jiang, A. Saxena, B. Song, B. B. Ward, T. J. Beveridge and S. C. B. Myneni, *Langmuir*, 2004, **20**(26), 11433–11442.

39 M. D. Guillén and N. Cabo, *J. Am. Oil Chem. Soc.*, 1997, **74**(10), 1281–1286.

40 Y. Y. Wang, J. Q. Li, H. G. Liu and Y. Z. Wang, *Molecules*, 2019, **24**(12), 2210.

41 J. Kong and S. Yu, *Acta Biochim. Biophys. Sin.*, 2007, **39**(8), 549–559.

42 A. D. Meade, C. Clarke, F. Draux, G. D. Sockalingum, M. Manfait, F. M. Lyng and H. J. Byrne, *Anal. Bioanal. Chem.*, 2010, **396**(5), 1781–1791.

43 S. Kalmodia, S. Parameswaran, W. Yang, C. J. Barrow and S. Krishnakumar, *Sci. Rep.*, 2015, **5**, 16649.

44 C. Weidenmaier and J. C. Lee, in Structure and Function of Surface Polysaccharides of Staphylococcus aureus, *Staphylococcus aureus: Microbiology, Pathology, Immunology, Therapy and Prophylaxis*, ed. F. Bagnoli, R. Rappuoli, G. Grandi, Springer International Publishing, Cham, 2017, pp. 57–93.

45 H. Xu, F. Qu, H. Xu, W. Lai, Y. Andrew Wang, Z. P. Aguilar and H. Wei, *BioMetals*, 2012, **25**(1), 45–53.

46 B. Ezraty, A. Gennaris, F. Barras and J.-F. Collet, *Nat. Rev. Microbiol.*, 2017, **15**(7), 385–396.

47 W. Vollmer, D. Blanot and M. A. De Pedro, *FEMS Microbiol. Rev.*, 2008, **32**(2), 149–167.

48 T. J. Silhavy, D. Kahne and S. Walker, *Cold Spring Harbor Perspect. Biol.*, 2010, **2**(5), a000414.

49 Q. L. Feng, J. Wu, G. Q. Chen, F. Z. Cui, T. N. Kim and J. O. Kim, *J. Biomed. Mater. Res.*, 2000, **52**(4), 662–668.

50 D. Inbakandan, C. Kumar, M. Bavanilatha, D. N. Ravindra, R. Kirubagaran and S. A. Khan, *Microb. Pathog.*, 2016, **99**, 135–141.

51 Z. Xu, C. Zhang, X. Wang and D. Liu, *ACS Appl. Bio Mater.*, 2021, **4**(5), 3985–3999.